https://doi.org/10.5194/egusphere-2026-3661
Preprint. Discussion started: 7 July 2026

# How tropical cyclones drive extreme positive glacier mass balance in the central–eastern Himalayas

Fengying Zhang[a,b], Xuelin Gao[a,b], Shihang Bai[b,e], Ji Zhang[a,b], Jing Gao[c], Rinzin Lhamo[f], Meilin Zhu[b,*], Huabiao Zhao[c,d,*]

[a]College of Earth and Environmental Sciences, Lanzhou University, Lanzhou, 730000, China

[b]Center for the Pan-third Pole Environment, Lanzhou University, Lanzhou, 730000, China

[c]State Key Laboratory of Tibetan Plateau Earth System, Environment and Resources, Institute of Tibetan Plateau Research, Chinese Academy of Sciences, Beijing, 100101, China

[d]Ngari Station for Desert Environment Observation and Research, Institute of Tibetan Plateau Research, Chinese Academy of Sciences, Xizang, 859700, China

[e]College of Atmospheric Science, Lanzhou University, Lanzhou, 730000, China

[f]Xizang Ngari Rutog County Meteorological Bureau, Xizang, 859700, China

Correspondence to Meilin Zhu (zhuml@lzu.edu.cn) and Huabiao Zhao (zhaohb@itpcas.ac.cn)

**Abstract.** Extreme climate events are increasingly recognized as important drivers of glacier change. Although tropical cyclones (TCs) are a type of extreme weather event, their impacts on glacier mass balance and the associated physical processes remain poorly understood. This study used more than 10 years of in situ observational data and an energy–mass balance model to reconstruct the energy and mass balance of Naimona'nyi Glacier over 2000–2024, and analyzed the impacts of TC Tauktae on glacier mass balance and associated physical mechanisms in May 2021. During May 18–21, 2021, meteorological and energy conditions changed markedly. Precipitation reached its highest level for the same period since 2000 and occurred almost entirely as snowfall, enhancing mass accumulation and surface albedo. Meanwhile, increased cloud cover reduced incoming shortwave radiation, and higher relative humidity decreased latent heat flux. These variations reduced melt energy, suppressed melt and sublimation, and increased mass accumulation, resulting in an extreme positive glacier mass balance for four consecutive days. Regional analysis shows that the associated meteorological and energy anomalies extended across the central and eastern Himalayas. This study reveals the physical mechanisms through which TCs drive glacier change on the Tibetan Plateau from an energy-balance perspective, filling a research gap in this area and providing important insights for regional glacier assessment and future projections.

https://doi.org/10.5194/egusphere-2026-3661
Preprint. Discussion started: 7 July 2026

## 1 Introduction

The Tibetan Plateau (TP) contains the largest concentration of glaciers in the middle and low latitudes of the world and plays a crucial role in supplying water to Asian inland rivers, maintaining regional ecological security, and supporting downstream socioeconomic development (Gao et al., 2019; Kääb et al., 2012; Milner et al., 2017; Yao et al., 2004, 2022). In recent decades, under global climate warming, glaciers across the TP have shown a persistent retreat trend (Davies et al., 2014; Duan et al., 2022; Vuille et al., 2008; Wang et al., 2019; Yang et al., 2013; Yao et al., 2012; Zhu et al., 2022). Meanwhile, the frequency and intensity of extreme climate events, such as heatwaves, have been increasing, making a non-negligible contribution to glacier mass loss (Chen et al., 2024; Kropač et al., 2021; Luo et al., 2026; Mote, 2014; Thibert et al., 2018; White et al., 2023; Xu et al., 2024; You et al., 2025; Zhu et al., 2024). Consequently, current studies on glacier change have mainly focused on negative mass balance processes. However, relatively less attention has been paid to events that may induce positive glacier mass balance. Positive mass balance processes are also important components of glacier evolution, influencing glacier mass balance states and potentially regulating regional hydrological processes. Therefore, investigating such processes is essential for a comprehensive understanding and accurate assessment of glacier mass balance changes.

Positive glacier mass balance is typically closely associated with processes such as snowfall, low air temperature, and cloud cover conditions (Fujita and Ageta, 2000; Kang et al., 2009; Zhang et al., 2021; Zhu et al., 2022, 2023, 2026b). Snowfall not only directly increases glacier mass accumulation, but also enhances glacier surface albedo, thereby reducing energy input (Fujita and Ageta, 2000). Low air temperature alters precipitation phase partitioning, causing more precipitation to fall as snow rather than rain, which further enhances accumulation and strengthens albedo feedback effects (Jouberton et al., 2022; Zhu et al., 2022). In addition, changes in cloud cover can modulate surface energy processes, thereby influencing glacier mass balance (Conway and Cullen, 2016). In real weather conditions, these factors do not act independently but instead influence glacier energy and mass balance through complex synergistic or compensating interactions. However, most studies on glacier mass balance have focused on single driving factors. While such approaches help identify the individual contributions of meteorological variables, they do not fully capture how multiple factors interact to jointly control glacier mass balance during integrated weather events, which remains poorly understood.

A tropical cyclone (TC) originates over tropical oceans and is driven principally by heat transfer from the ocean (Emanuel, 2003). It can transport large amounts of water vapour and trigger intense precipitation within its circulation. Therefore, in affected regions, TC-related precipitation can account for a substantial proportion of total annual precipitation and exert a significant influence on regional meteorological conditions (Dare et al., 2012; Khouakhi et al., 2017; Ren et al., 2006). Glaciers are highly sensitive to climate variability. However, how TCs influence glacier mass balance through the combined effects of multiple meteorological variables, as well as the underlying physical mechanisms, remains insufficiently understood in the TP. This limits a comprehensive understanding of the role of such complete weather systems in glacier change.

Tropical cyclone Tauktae formed over the Arabian Sea on May 14, 2021, and made landfall along the coast of Gujarat in western India on May 17, 2021. It was one of the most severe cyclonic events in recent years, causing the deaths of at least 12 people, destroying hundreds of homes, and resulting in power outages and traffic jams (Kannaujiya et al., 2024). After landfall, its residual moisture continued to move northward and triggered a significant snowfall event over the western TP, particularly affecting Zanda, Burang, and Gar counties. Naimona'nyi Glacier is located in Burang County on the northern slope of the Himalayas in the southwestern TP. Continuous glacier mass balance and meteorological observations have been conducted in this region for more than a decade, providing valuable long-term observational data for investigating the impacts of TC events on glacier change. Building on these observations, this study focuses on Naimona'nyi Glacier and combines long-term observations with an energy and mass balance model to analyze the meteorological variations, the energy and mass balance response to the TC Tauktae event in May 2021. The objectives of this study are to (1) determine whether a TC event can induce a positive glacier mass balance and (2) clarify the mechanisms through which such events influence glacier mass balance. The results are expected to improve understanding of how TC events affect glacier energy and mass balance processes and to provide scientific support for future glacier change projections, glacier hazard assessment, and alpine water resource management.

## 2 Study Area and Data

### 2.1. Study Area

Naimona'nyi Glacier is located in the southwestern TP (Fig. 1). As one of the largest glaciers in the Mount Naimona'nyi region, it consists of southern and northern branches. Meltwater from the northern branch drains into the Majiazangbu River, a tributary of the Ganges, and runoff from the southern branch flows into Lake Manasarovar. This study focuses specifically on the northern branch. The glacier covers an area of 7.34 km² and spans an elevation range from 5400 to 7400 m above sea level (a.s.l.), with approximately 90% of its area located below 6200 m a.s.l. (Guo et al., 2015). The region is jointly influenced by the Indian summer monsoon and the westerlies; the former dominates in summer, whereas the latter prevails in winter (Yao et al., 2012). Meteorological records from an automatic weather station (AWS) at 5,910 m a.s.l. on the slopes north of the glacier indicate a mean annual air temperature of –6.0 °C, with the highest monthly temperatures occurring in July. Annual precipitation averages 292.5 mm and exhibits a bimodal distribution (Zhu et al., 2021). In recent decades, Naimona'nyi Glacier has experienced marked mass loss, with a mean annual mass balance of approximately –390 mm w.e. $a^{-1}$ during 2011–2018 (Zhu et al., 2021). Mass loss occurs predominantly during the ablation season, while the glacier remains near a balanced condition during the cold season (Zhu et al., 2021).

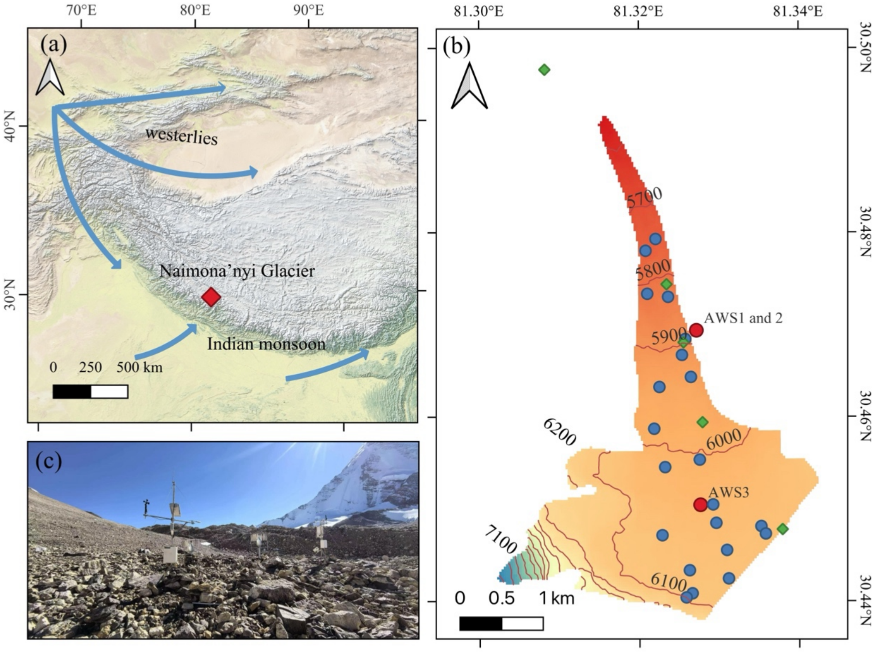

**Figure 1: (a) Location of Naimona'nyi Glacier. (b) Contour map showing mass balance stakes (blue circles),**

https://doi.org/10.5194/egusphere-2026-3661
Preprint. Discussion started: 7 July 2026

**air temperature probes (green diamonds), and AWSs (red circles). (c) Photograph of AWS1.**

## 2.2. Field measurements

Three automatic weather stations (AWSs) were installed at different altitudes on and around Naimona'nyi Glacier (Fig. 1b). Two stations (AWS1 and 2) were placed on a hillside north of the glacier at an elevation of 5910 m a.s.l. (Fig. 1b). AWS1 began operation in October 2011 and measured air temperature ($T_a$), relative humidity (RH), wind speed (WS), wind direction (WD), and incoming shortwave radiation ($S_{in}$) at half-hourly resolution. Due to instrumental issues, all measurements from AWS1 were unavailable between April and September 2012. In addition, Ta and RH measurements were missing from January to September 2013 because the temperature and humidity sensor detached from its radiation shield. Precipitation data were obtained from all-weather precipitation gauges (T-200B) equipped with hanging weighing transducers, which were installed close to AWS1 in September 2013. AWS2 was installed near AWS1 in October 2021 and has recorded WD, WS, $T_a$, RH, air pressure, $S_{in}$, outgoing shortwave radiation ($S_{out}$), incoming longwave radiation ($L_{in}$), and outgoing longwave radiation ($L_{out}$) at half-hourly resolution since October 11, 2021.

AWS3 (6039 m a.s.l.) was installed on the glacier surface. It recorded meteorological variables at 10 Hz from October 2023 to October 2024, including $T_a$, RH, WS, WD, $S_{in}$, $S_{out}$, $L_{in}$, and $L_{out}$. A WindMaster Pro three-dimensional sonic anemometer (Gill Instruments Ltd.) and a LI-7500DS Open Path CO2/H2O Analyzer (Li-Cor Inc.) were used to measure eddy-covariance turbulence. All raw turbulence data were collected at 10 Hz, including the three wind velocity components, virtual temperature, and water vapor concentrations. Observations from AWS3 were used to evaluate the accuracy of the model simulations. Details of the sensors used for each variable are provided in Table S1.

Glacier mass balance on the northern branch of Naimona'nyi Glacier has been measured using the glaciological method since 2004 (Zhao et al., 2016; Zhu et al., 2021). The number of monitoring stakes distributed across the entire glacier surface increased progressively from 4 in 2004 to 31 in 2013 (Zhao et al., 2016; Zhu et al., 2021). Some stakes lost due to glacier surface melt or were damaged by animals, and some measurements failed because of extremely bad weather. Nevertheless, after the 2013/2014 mass balance year (defined as October of the previous year to September of the current year), our observation network provided at least 10 point mass balance measurements per year. Fieldwork was not conducted in 2015 or 2022 because of logistical constraints. However, point measurements were obtained in October 2016 and November 2023. These measurements allowed us to calculate glacier-wide mass balance for the extended periods of 2014–2016 and 2021–2023, respectively. The stakes were distributed between 5750 and 6130 m a.s.l., as the glacier is inaccessible above 6130 m a.s.l. (Fig. 1b). In early November of each study year, we manually recorded stake heights and snow-pit features (snow layer density and stratigraphy) to derive annual point mass balance. Annual glacier-wide mass balance was calculated following the method of Zhu et al. (2021).

### 2.3. Other data

We additionally used the fifth-generation reanalysis data from the European Centre for Medium-Range Weather Forecasts (ERA5), including Ta, RH (derived from dew point temperature and air temperature), WS, precipitation, and $S_{in}$, to reconstruct a continuous hourly meteorological dataset covering the period from July 1, 1994, to September 30, 2024. Data from July 1, 1994, to September 30, 1999, were used for model spin-up. ERA5 has a horizontal resolution of 0.25° × 0.25° and has been widely used in climate research.

## 3 Methods

### 3.1. The energy and mass balance model

In this study, we use the coupled energy and mass balance firn model (EBFM), which consists of a surface energy balance model and a subsurface model that describes the evolution of vertical profiles of temperature, density, and water content (van Pelt et al., 2012, 2019). The energy and mass balance model employed here is described in detail in van Pelt et al. (2012); therefore, we only present the main features of the model. The mass balance is calculated as follows:

$$MB = C_{en} + P_{snow} + M_{water} + E_v \qquad (1)$$

where point mass balance (MB) consists of refreezing ($C_{en}$), snowfall ($P_{snow}$), melting ($M_{water}$), and sublimation/evaporation ($E_v$). Melt energy (QM) is calculated from the surface energy balance equation:

$$Q_M = S_{in} + S_{out} + L_{in} + L_{out} + H_{sen} + H_{lat} + G \qquad (2)$$

where $H_{sen}$ is the sensible heat flux, $H_{lat}$ is the latent heat flux, and G is the conductive heat flux. $Q_M$ is defined as positive when it exceeds zero. The surface energy balance module calculates the surface temperature by iteratively solving the energy balance equation. When the calculated surface temperature exceeds the melting point of ice (0 °C), it is constrained to 0 °C, and the surplus energy is used for snow and ice melt. Energy fluxes directed toward the glacier surface are defined as positive, whereas fluxes leaving the surface are defined as negative.

The model was run at an hourly time step with a spatial resolution of 90 × 90 m from October 1999 to September 2024. The meteorological forcing data, including $T_a$, RH, WS, precipitation, and cloud cover from AWS1, were used to drive the EBFM model. Air temperature was interpolated across the glacier using a lapse rate of $-0.69$ °C 100 $m^{-1}$ above 5919 m a.s.l. and $-0.84$ °C 100 $m^{-1}$ below 5919 m a.s.l., derived from five air temperature and humidity probes on the glacier and AWS1. Precipitation was interpolated using two different elevation-dependent gradients. Above 5800 m a.s.l., a gradient of 8.6% 100 $m^{-1}$ was applied based on observations from AWS2 and the Burang meteorological station during October 2013 to September 2018 (Zhu et al., 2021). Below 5800 m a.s.l., a gradient of 2% 100 $m^{-1}$ was used, which was adjusted to ensure that the EBFM model simulations achieved satisfactory performance. Wind speed and RH from AWS1 were assumed to be spatially homogeneous, as observations on the glacier were too sparse to develop a reliable elevation-dependent parameterization (Fujita and Ageta, 2000; Hock and Holmgren, 2005). Air pressure at each grid point was calculated using an exponential decay with elevation. Cloud cover was estimated as the ratio of $S_{in}$ to the top-of-atmosphere (TOA) radiation. Energy balance components (e.g., $S_{in}$, $S_{out}$, $L_{in}$, and $L_{out}$) and mass balance components (e.g., snowfall and melting) were calculated using physically based parameterizations. Detailed information about the EBFM model is provided in Text S1, and the input parameters are listed in Table S2.

The densities of fresh snowfall and ice were assumed to be 200 and 900 kg $m^{-3}$, respectively. For each grid cell on Naimona'nyi Glacier, the temperature at ice depth was estimated using the multi-annual mean air temperature recorded at AWS1 (Zhu et al., 2021). The initial snow depth was set to 0.03 m w.e. for all grid cells, with an initial snow density of 200 kg $m^{-3}$. To eliminate the influence of initial condition uncertainties on model results, a spin-up procedure was performed prior to the main simulations. The model was forced with data starting from July 1, 1994, but the analysis focuses primarily on the period

https://doi.org/10.5194/egusphere-2026-3661
Preprint. Discussion started: 7 July 2026

from October 1999 to September 2024. Most physical parameters used in the EBFM model were derived from in situ measurements and published literature. Only the parameters of the albedo model and the precipitation gradient below 5800 m a.s.l. were adjusted to achieve the best agreement between the modelled and measured mass balance (considering both glacier-wide and stake-specific values) and albedo data during the 2000–2024 period (from October 1999 to September 2024).

### 3.2. Data processing

To obtain continuous meteorological data from October 1999 to September 2024, gaps in the hourly time series of $T_a$, WS, RH, precipitation, and $S_{in}$ at AWS1 were filled using the downscaled ERA5 data. Monthly and hour-specific linear regression relationships were established between ERA5 data and AWS1 observations, following the method of Zhu et al. (2026). These relationships were then applied to correct the ERA5 data, generating continuous time series of the above variables. Prior to regression, anomalous AWS1 observations were removed, including WS $\leq 0$ m s$^{-1}$, RH $< 0\%$ or RH $> 100\%$, and $S_{in}$ exceeding the solar constant (1361 W m$^{-2}$). For $S_{in}$, only daytime periods with non-zero radiation values were considered. Monthly and hour-specific regression relationships were developed to reconstruct the $S_{in}$ time series. Comparisons between the reconstructed and observed meteorological variables demonstrate the reliability of the reconstructed $T_a$, WS, RH, and $S_{in}$ (Fig. S1). Precipitation reconstruction was achieved by matching both the occurrence frequency and total precipitation between ERA5 data and AWS1 observations (Zhu et al., 2021). A precipitation threshold was first determined; ERA5 values below this threshold were set to zero to align the frequency of precipitation events with observations. A scaling factor, calculated as the ratio of total observed precipitation to total ERA5 precipitation, was then applied to the ERA5 data to produce a complete precipitation time series. The cumulative number of precipitation events, total precipitation amount, and monthly precipitation from the reconstructed data show good agreement with observed values (Fig. S2). Figure S3 presents the data ($T_a$, RH, WS, precipitation, $S_{in}$, and cloud cover) that were used to run the EBFM model for the glacier.

### 3.3. Model calibration and uncertainty analysis

To evaluate the performance of the EBFM model, simulated results were compared with observed data for several variables. The model was calibrated using data measured at AWS1 and 2, and validated using

https://doi.org/10.5194/egusphere-2026-3661
Preprint. Discussion started: 7 July 2026

data measured at AWS3 (Fig. 2). The evaluation variables included daily mean $S_{in}$ from July 2012 to October 2024 at AWS1; daily mean $L_{in}$ from October 2021 to October 2024 at AWS2; and daily mean glacier surface temperature, surface albedo, $L_{in}$, $H_{sen}$, and $H_{lat}$ from November 2023 to October 2024 at AWS3 (Fig. 2). The root mean square error (RMSE) and correlation coefficient (R) between simulated and measured $L_{in}$ at AWS2 were 15.5 W m$^{-2}$ and 0.96, respectively (Fig. 2a). For surface albedo at AWS3, the RMSE was 0.1 and R was 0.5 (Fig. 2b). The main discrepancies occurred in late winter, from late February to mid-to-late March 2024, when frequent blowing snow events significantly reduced the observed albedo. This likely introduced a warm bias in the simulated surface temperature. However, because these deviations occurred during the non-ablation season, their impact on the overall representativeness and reliability of the simulation is considered limited. For glacier surface temperature at AWS3, the RMSE and R values were 3.2 °C and 0.98, respectively (Fig. 2c). For $L_{in}$ at AWS3, the RMSE and R values were 19.6 W m$^{-2}$ and 0.95, respectively (Fig. 2d). The turbulent heat flux data measured by the eddy covariance system were also used to verify the calculated fluxes (Fig. 2e and 2f). The RMSE between the modelled and observed $H_{sen}$ values at AWS3 was 19.9 W m$^{-2}$, and the corresponding R was 0.7. The RMSE between the modelled and observed $H_{lat}$ values at AWS3 was 9.9 W m$^{-2}$, and the corresponding R was 0.71. The simulated turbulent fluxes were in good agreement with the direct measurements. Overall, the agreement between modelled and measured variables is good, despite some discrepancies during certain periods, indicating that the simulation performed well.

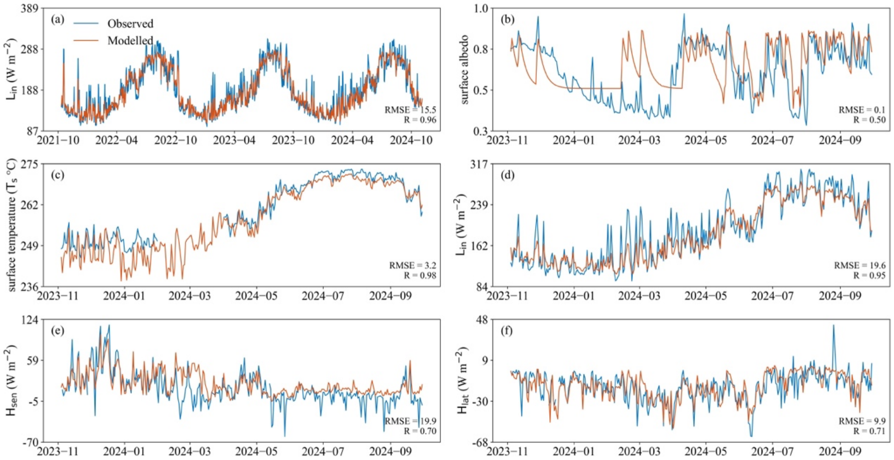

**Figure 2: In situ measurements and model results for energy balance components. (a) Comparison between**

https://doi.org/10.5194/egusphere-2026-3661
Preprint. Discussion started: 7 July 2026

**observed and simulated incoming longwave radiation ($L_{in}$, W $m^{-2}$) at AWS2 during 2021–2024. (b–f) Comparison between observed and simulated surface energy balance variables at AWS3 from December 2023 to September 2024, including (b) surface albedo, (c) surface temperature ($T_s$, °C), (d) incoming longwave radiation ($L_{in}$, W $m^{-2}$), (e) sensible heat flux ($H_{sen}$, W $m^{-2}$), and (f) latent heat flux ($H_{lat}$, W $m^{-2}$).**

In addition, the model was evaluated using stake mass balance measurements from multiple observational periods within each mass balance year. Figure 3 shows the modelled and measured annual mass balance at different elevations. Over the period 2009–2024, the RMSE between observed and modelled mass balance at all stakes ranged from 0.17 to 0.89 m w.e. $a^{-1}$, with a mean value of 0.37 m w.e. $a^{-1}$; the R between observed and modelled mass balance at all stakes ranged from 0.82 to 0.97, with a mean value of 0.91. This performance is slightly better than that reported in Zhao et al. (2016) and Zhang et al. (2018), indicating generally good agreement between observations and simulations at the stake scale. A discernible underestimation of modelled mass balance occurred during the 2013/2014 mass balance year across different altitudes. This underestimation may be related to anomalous snowfall frequency and amount, which led to lower albedo and consequently higher melt. Additionally, the complex topography and snowdrift effects can cause high spatial variability in precipitation and its gradient across the glacier surface (Zhang et al., 2012). These factors can introduce spatial heterogeneity in mass balance at the same altitude by modifying albedo, melt energy, and accumulation, thereby explaining the mismatches between measured and modelled mass balance at some locations (Fig. 3). Overall, this analysis demonstrates that the model is capable of capturing changes in glacier mass balance. Therefore, the simulation results can be used to analyze the response of glacier mass and energy balance to extreme weather and climate events.

Uncertainty in the model results is primarily associated with key parameters, including snow albedo, firn albedo, ice albedo parameters, precipitation gradient, critical temperature, and turbulent flux parameters, as their prescribed values can strongly influence model outputs. The uncertainty associated with each parameter was quantified by perturbing its value by ±10%, while keeping other parameters unchanged. This method has been widely used in glacier modelling (Zhu et al., 2021). Given that our study focuses on glacier mass balance change from May 18–21, 2021, we assess uncertainties in the modelled mass balance over this period arising from parameter perturbations. The calculated uncertainties for each parameter are listed in Table S2 of Supporting Information S1. Among all tested parameters, fresh snow albedo in the albedo scheme showed the highest sensitivity (Table S3). The average uncertainty in the modelled glacier mass balance during May 18–21, 2021, and for the same period since 2000 were 0.11 and 0.15 mm w.e. d$^{-1}$, respectively, estimated using the error propagation method described by Zhu et al. (2021).

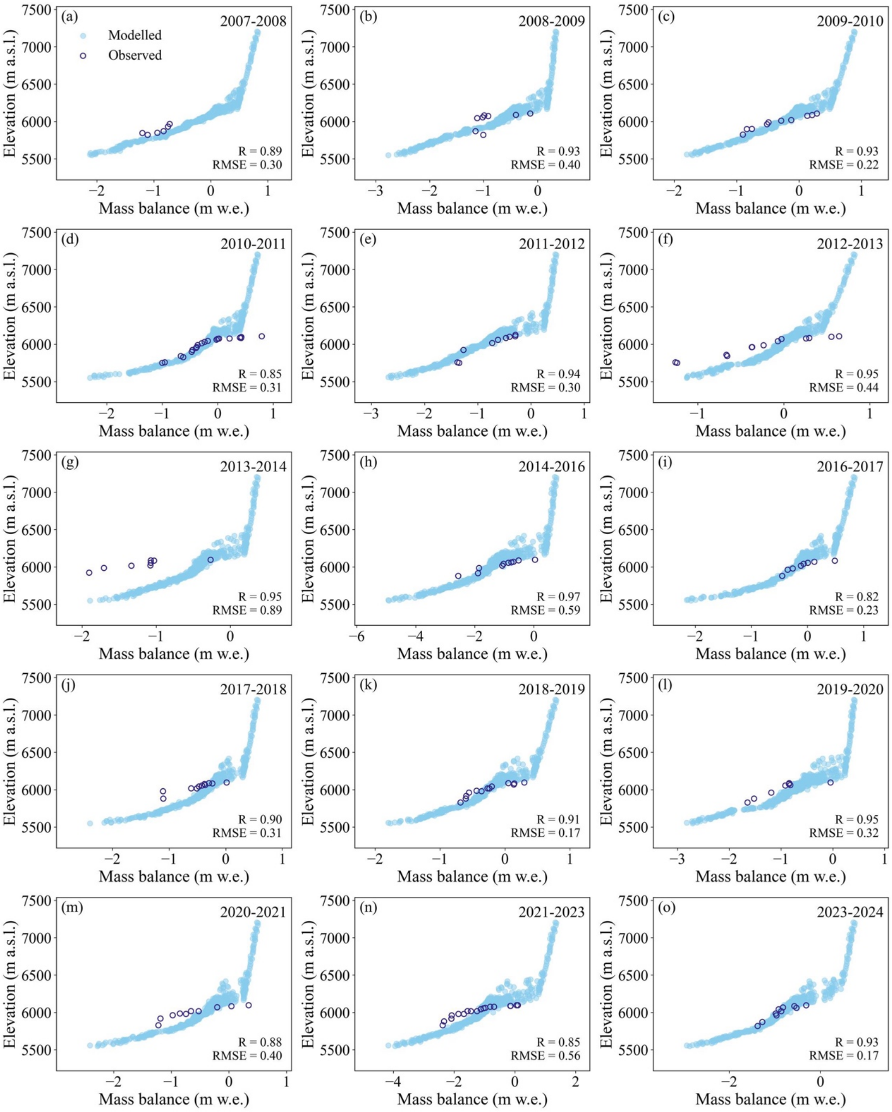

**Figure 3: Comparison of modelled and observed glacier mass balance across different elevations from 2008 to 2024. Blue dots represent modelled mass balance values, while open circles denote field observations. The correlation coefficient (R) and root mean square error (RMSE) are shown in each panel to evaluate model**

https://doi.org/10.5194/egusphere-2026-3661
Preprint. Discussion started: 7 July 2026

**performance.**

## 4. Results

### 4.1 Meteorological conditions during the tropical cyclone Tauktae influence period

Tropical cyclone Tauktae made landfall on May 17, 2021, along the coast of the western Indian state of Gujarat. The residual moisture subsequently propagated northeastward, leading to substantial precipitation over Ngari Prefecture. Therefore, meteorological observations from May 18, 2021, onward were selected for analysis. As shown in Fig. S4, meteorological conditions such as precipitation and $T_a$ exhibited pronounced variability during May 18–21, 2021. Accordingly, we defined May 18–21, 2021, as the TC influence period (TC period). In addition, the multi-year mean for the same period from 2000 to 2024 was used as a reference for comparison and defined as the baseline period for subsequent analysis. The percentile threshold method is widely used to define extreme events in meteorological studies (DeGaetano and Allen, 2002; Nerantzaki and Papalexiou, 2022; Schär et al., 2016). This study adopts this method and defines values exceeding the 90th percentile as extreme conditions, in order to reveal the anomalous meteorological characteristics during the TC period.

Precipitation increased markedly during the TC period, with a mean daily precipitation of 5.6 mm, compared to only 0.85 mm during the baseline period, representing an increase of 4.75 mm $d^{-1}$. In terms of precipitation frequency, the total number of precipitation hours during the TC period reached 80, approximately four times higher than that during the baseline period. As the event occurred in May, air temperatures at high elevations were relatively low, resulting in only minor differences in precipitation phase between the two periods. Snowfall accounted for 99.98% and 99.86% of total precipitation during the TC and baseline periods, respectively. To further assess the extremity of the event, daily precipitation during the TC period was ranked against records from the same calendar period during 2000–2024. The results showed that the mean daily precipitation during the TC period reached the highest value in the record, making it the most extreme precipitation event for the same calendar period over the past 25 years. In addition, compared with other precipitation events from March to May 2021 (Fig. S5), daily precipitation during most periods was generally below 2.5 mm, except for April 21–24, 2021, and May

28–29, 2021. Moreover, intense precipitation events typically persisted for less than three days. In contrast, during the TC period, daily precipitation exceeded 3 mm for four consecutive days, indicating both higher precipitation intensity and longer duration. Therefore, relative to the baseline period, the TC period was characterized by substantial increases in both precipitation frequency and intensity, reaching an extreme level for the historical period. Compared with other precipitation events in spring 2021, the precipitation also exhibited a longer duration and greater precipitation intensity.

During the TC period, RH increased markedly, with a daily mean of 73%, which was 21% higher than that during the baseline period and corresponded to the 92nd percentile (Fig. 4e). Wind speed also showed a marked increase, with an average of 8.7 $\text{m s}^{-1}$, 4.8 $\text{m s}^{-1}$ higher than the baseline period, reaching the 100th percentile (Fig. 4b). Cloud cover during the TC period daily averaged 42.5%, which was 1% higher than during the baseline period, corresponding to the 64th percentile (Fig. 4c). Air temperature averaged −6.0 °C, 1.9 °C higher than the baseline period, reaching the 96th percentile (Fig. 4d). Surface temperature daily averaged −8.4 °C, which was 4.23 °C higher than that during the baseline period and reached the 100th percentile (Fig. 4f). Overall, the TC period was characterized by pronounced changes in meteorological conditions, with RH, WS, $T_a$, and $T_s$ all reaching the highest values in the historical record, while cloud cover remained slightly higher than the baseline period average.

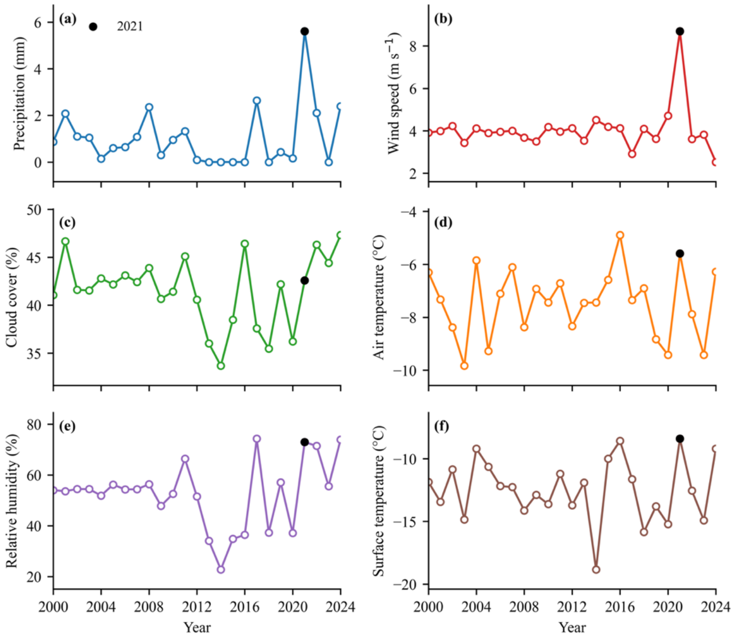

**Figure 4: Interannual variability of meteorological variables during 18–21 May (2000–2024). (a) Precipitation (mm), (b) wind speed (WS, m s$^{-1}$), (c) cloud cover (%), (d) air temperature ($T_a$, °C), (e) relative humidity (RH, %) and (f) surface temperature ($T_s$, °C). All variables represent averages during May 18–21 of each year. The black dots indicate values in 2021. The dashed black lines represent the mean of the baseline period (2000–2024).**

## 4.2 Mass balance and flux variations during the tropical cyclone period

Figure 5a shows the mass balance and its fluxes during the TC period and the baseline period, including mass balance, snowfall, refreezing, sublimation, and melting. During the TC period, glacier mass balance remained positive for four consecutive days (Fig. S4a), with a mean daily value of 4.87 mm w.e. d$^{-1}$, which is approximately 6.17 mm w.e. d$^{-1}$ higher than that in the baseline period and 1.72 times the standard deviation (Fig. 5a). At the diurnal scale, a slight negative value occurred only around 16:00 during the TC period, while the remainder of the day stayed positive. In contrast, during the baseline period, mass balance remained negative from 11:00 to 19:00 (Fig. S6). Percentile analysis shows that mass balance during the TC period reached the highest value in the 2000–2024 record (Fig. 5f), indicating an exceptionally extreme positive mass balance event.

Spatially, the TC event substantially altered the vertical pattern of glacier mass balance. During the baseline period, areas below 6200 m a.s.l. were predominantly characterized by negative mass balance, while only higher elevations (>6200 m a.s.l.) exhibited weakly positive values (Fig. 6b). In contrast, during the TC period, the entire glacier maintained positive mass balance (Fig. 6a). These results indicate that the TC event not only increased the magnitude of mass balance but also expanded the extent of positive balance from high elevations to the entire glacier.

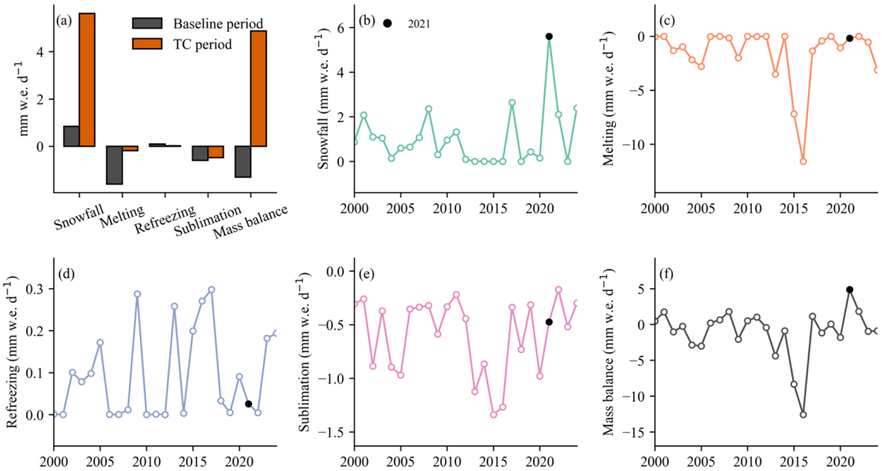

**Figure 5: Comparison of glacier mass balance and fluxes during the TC period (May 18–21, 2021), the baseline period (2000–2024), and interannual variability over the same calendar window. (a) Mean daily snowfall, melting, refreezing, sublimation, and mass balance during the TC period and the baseline period. (b–f) Interannual variations of each component averaged over May 18–21 for 2000–2024. (b) Snowfall (mm w.e. d⁻¹), (c) melting (mm w.e. d⁻¹), (d) refreezing (mm w.e. d⁻¹), (e) sublimation (mm w.e. d⁻¹), and (f) mass balance (mm w.e. d⁻¹). The black dot highlights the year 2021 (TC period).**

To investigate the causes of the pronounced increase in mass balance, the mass balance fluxes during the TC period were further compared with those during the baseline period (Fig. 5). The results show that, in terms of mass accumulation, snowfall during the TC period reached 5.6 mm w.e. d$^{-1}$, compared to approximately 0.8 mm w.e. d$^{-1}$ during the baseline period, representing an increase of 4.8 mm w.e. d$^{-1}$ and reaching the highest snowfall for the same period during 2000–2024. Refreezing was 0.095 mm w.e. d$^{-1}$, about 0.07 mm w.e. d$^{-1}$ lower than that during the baseline period (Fig. 5d). In terms of mass loss, both melting and sublimation were reduced. Melting was 0.2 mm w.e. d$^{-1}$, 1.4 mm w.e. d$^{-1}$ lower than that during the baseline period (Fig. 5c), while sublimation decreased from 0.59 to 0.47 mm w.e. d$^{-1}$, a decrease of 0.12 mm w.e. d$^{-1}$ (Fig. 5e). Therefore, the positive mass balance during the TC period was primarily driven by extremely high snowfall together with reduced melting and sublimation.

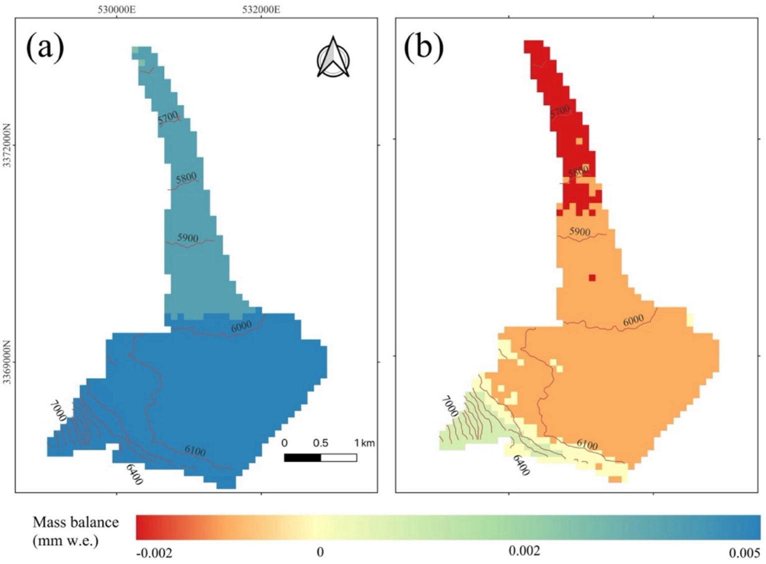

**Figure 6: Spatial distribution of daily mean glacier mass balance during (a) the TC period, and (b) the baseline period.**

### 4.3 Mechanisms driving changes in glacier mass balance during the tropical cyclone period

We analyzed the energy flux characteristics during the TC and baseline periods. Figure 7a shows the variations in energy fluxes for the two periods, including $S_{in}$, $S_{out}$, $L_{in}$, $L_{out}$, G, $H_{lat}$, $H_{sen}$, and QM. The results indicate a pronounced difference in QM magnitude between the TC and baseline periods. The mean daily QM during the TC period was 0.71 W m$^{-2}$, which was about 5.4 W m$^{-2}$ lower than the 6.09 W m$^{-2}$ during the baseline period. The relative contributions of $S_{in}$, $S_{out}$, $L_{in}$, $L_{out}$, $H_{sen}$, G, and $H_{lat}$ to the surface energy balance during the TC period are 27.0%, −22.5%, 20.5%, −25.6%, 2.6%, −0.3%, and −1.4%, respectively, whereas the corresponding values during the baseline period were 30.2%, −21.9%, 18.5%, −25.4%, 1.6%, −0.4%, and −1.8%. Overall, both periods exhibit an energy balance dominated by shortwave and longwave radiation, with $S_{in}$ and $L_{in}$ acting as the main energy sources, and $L_{out}$ and $S_{out}$ as the primary energy sinks.

We further compared the energy fluxes and surface albedo differences between the TC and baseline periods to understand the mechanisms driving the decrease in QM, as shown in Fig. 7. During the TC period, $S_{in}$ dropped substantially by about 18.6 W m$^{-2}$ compared to the baseline period. At the same time,

$S_{out}$ increased by 19.0 W m⁻² due to higher surface albedo (Fig. 7a). Together, these changes reduced net shortwave radiation ($S_{net}$) by roughly 37.6 W m⁻². In contrast, $L_{in}$ during the TC period increased by about 32 W m⁻² relative to the baseline period. Outgoing longwave radiation also increased by about 16.5 W m⁻², resulting in a net increase of 15.5 W m⁻² in net longwave radiation ($L_{net}$). However, the enhancement in $L_{out}$ occurred predominantly during nighttime. During daytime, when melt processes were most active, $L_{out}$ was generally lower than during the baseline period (Fig. S7). Therefore, the increase in $L_{out}$ cannot be considered a major contributor to the reduction in QM. Meanwhile, the absolute value of $H_{lat}$ decreased by about 3.5 W m⁻² relative to the baseline period, while $H_{sen}$ increased markedly by about 11.5 W m⁻². Thus, even though the higher $L_{in}$ and $H_{sen}$ during the TC period contributed more energy to the glacier surface, the large drop in $S_{in}$ and the stronger energy losses through $S_{out}$ together controlled the energy changes, resulting in a significant reduction in QM.

To understand how TC affects glacier mass balance, we linked the meteorological conditions with the energy and mass balance processes and found that the impact of the TC event on glacier mass balance is mainly driven by the following mechanisms. First, increased cloud cover during the TC period led to a decrease in $S_{in}$ of about 18.6 W m⁻². Meanwhile, the additional snowfall increased the surface albedo, thereby enhancing $S_{out}$. The combined effect of these two processes results in a reduction in $S_{net}$ of approximately 37.6 W m⁻². Second, the reduced humidity gradients between the surface and the atmosphere weakened the $H_{lat}$. Finally, the substantially enhanced snowfall provided an additional mass input of approximately 5.6 mm w.e. d⁻¹. Under the combined influence of these mechanisms, QM was reduced and sublimation was suppressed, leading to a decrease in melting of about 1.4 mm w.e. d⁻¹ and a reduction in sublimation of about 0.12 mm w.e. d⁻¹, while mass accumulation increased by approximately 5.6 mm w.e. d⁻¹. Consequently, glacier mass balance during the TC period increased by about 6.17 mm w.e. d⁻¹ compared to that during the baseline period, shifting from negative to positive mass balance.

https://doi.org/10.5194/egusphere-2026-3661
Preprint. Discussion started: 7 July 2026

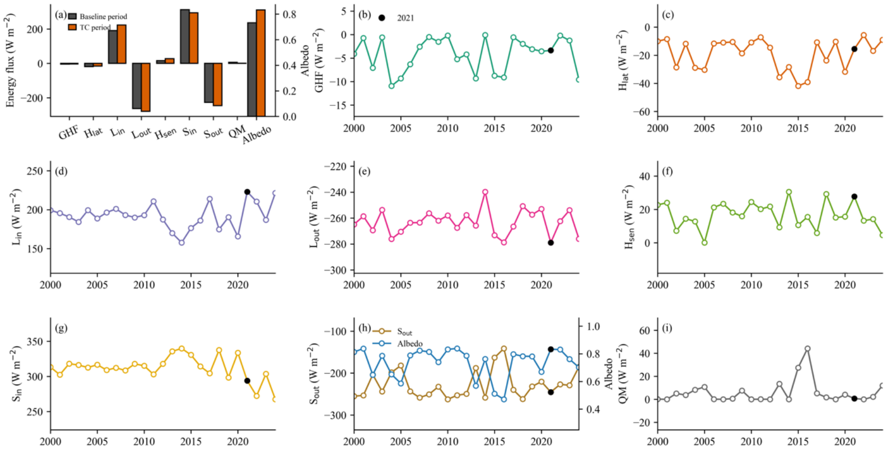

**Figure 7: Comparison of energy fluxes during the TC period (18–21 May 2021), the baseline period (2000–2024), and interannual variability over the same calendar window. (a) Mean daily Sin, Sout, Lin, Lout, Hsen, G, Hlat, and QM during the TC period and the baseline period. (b–i) Interannual variations of each component averaged over 18–21 May for 2000–2024. (b) G ($W\ m^{-2}$), (c) Hlat ($W\ m^{-2}$), (d) Lin ($W\ m^{-2}$), (e) Lout ($W\ m^{-2}$), (f) Hsen ($W\ m^{-2}$), (g) Sin ($W\ m^{-2}$), (h) Sout ($W\ m^{-2}$), and (i) QM ($W\ m^{-2}$). The black dot highlights the year 2021 (TC period).**

## 5. Discussion

### 5.1 Spatial extent of tropical cyclone Tauktae impacts over the Himalayas

North Indian Ocean tropical cyclones are an important component of global TC activity, primarily occurring in the Arabian Sea and the Bay of Bengal, and accounting for approximately 6% of global tropical cyclone activity (Ali, 1999). Their formation and evolution are controlled by local oceanic thermal conditions, and are also modulated by multi-scale climate variability (Bhardwaj et al., 2019; Felton et al., 2013; Krishnamohan et al., 2012; Singh et al., 2020; Singh and Roxy, 2022; VinodKumar et al., 2014). The genesis and rapid intensification of TC Tauktae resulted from the synergistic interaction between oceanic and atmospheric conditions, with anomalously warm ocean conditions playing a key role. Prior to its formation, sea surface temperature (SST) in the Arabian Sea increased persistently to 30–32 °C, with SST anomalies reaching 0.8–1.6 °C. The TC heat potential was as high as 120–140 kJ $cm^{-2}$, accompanied by elevated upper-ocean heat content and warm-core eddy activity, which provided a continuous and abundant energy supply for the TC. Meanwhile, high relative humidity, strong low-level absolute vorticity, weak vertical wind shear, and a high genesis potential index collectively created a highly favorable atmospheric environment for tropical cyclone development (Kannaujiya et al., 2024; Ratnakaran and Abish, 2023; Umakanth et al., 2024). In addition, La Niña conditions, a negative Indian Ocean Dipole (IOD), and an active Madden–Julian Oscillation (MJO) further enhanced moisture transport and low-level vorticity over the eastern Arabian Sea, providing additional support for cyclone formation and rapid intensification (Zahid and Harikumar, 2025). Under these exceptionally favorable ocean–atmosphere conditions, TC Tauktae underwent a marked and rapid intensification and ultimately became the strongest pre-monsoon cyclone over the Arabian Sea since TC Kandla in 1998.

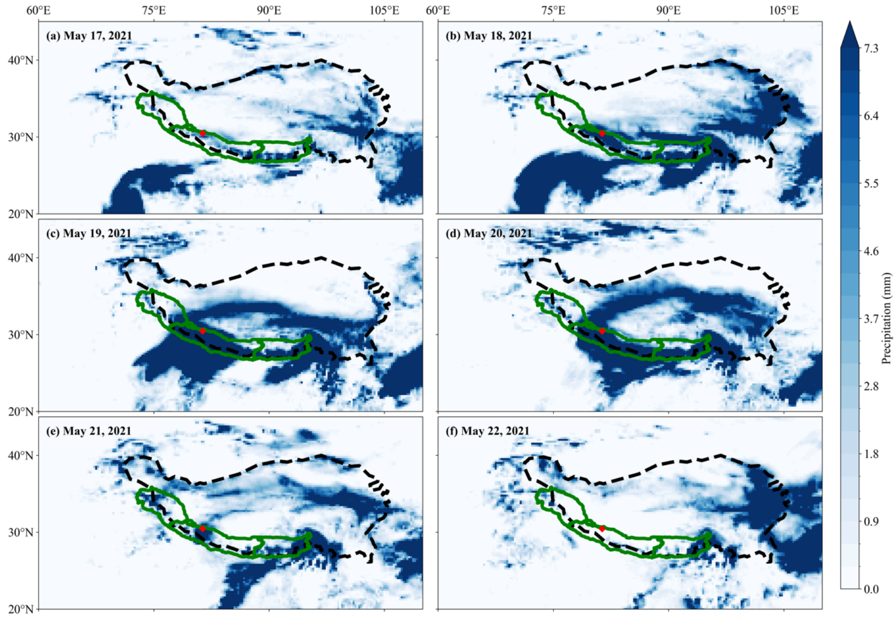

**Figure 8: Spatial distribution of daily precipitation from ERA5 data over the Tibetan Plateau and surrounding regions from May 17 to 22, 2021. Precipitation is shown using a blue color gradient, with darker shades indicating higher precipitation intensity. The black dashed line denotes the boundary of the Tibetan Plateau, while the green solid line represents the extent and subdivision of the Himalayas. The red diamond markers indicate the location of Naimona'nyi Glacier. Panels (a)–(f) correspond to May 17–22, 2021, respectively.**

The meteorological and energy changes induced by TC Tauktae are not confined to a single glacier. To further assess the spatial influence range of TC Tauktae, we analyzed daily precipitation (Fig. 8), snowfall (Fig. 9), albedo, RH, $S_{net}$, $S_{in}$ and cloud fraction from May 17 to 22, 2021, using ERA5 data (Fig. S8–

https://doi.org/10.5194/egusphere-2026-3661
Preprint. Discussion started: 7 July 2026

S12). The results showed a clear south-to-north progression of precipitation across the Himalayas during the TC period. As the cyclone moved inland, the affected area gradually expanded into the central and eastern Himalayas from May 18, 2021, onward. The precipitation reached its maximum extent and intensity during May 19–20, 2021, when it extensively covered the central and eastern Himalayan regions. By May 21, 2021, precipitation had weakened and the affected area retreated to the central Himalayas, and by May 22, 2021, with no significant precipitation remaining over the region. Relative humidity, $S_{net}$, $S_{in}$ and cloud fraction exhibited consistent spatiotemporal patterns (Fig. S9–12). From May 18 to 20, 2021, the affected area extended across the central and eastern Himalayas, while conditions began to weaken on May 21, 2021, and returned to near-normal by May 22, 2021. Surface albedo and snowfall increased over parts of the central-eastern Himalayas from May 18 to 20, 2021, and persisted until May 21, 2021 (Fig. S8). However, no pronounced increase in albedo was observed in the eastern Himalayas, which may be related to the differences in precipitation phase in this region. Integrating the spatial patterns of precipitation, snowfall, cloud fraction, RH, albedo and shortwave radiation, our results indicate that the influence of TC Tauktae primarily affected the central–eastern Himalayas.

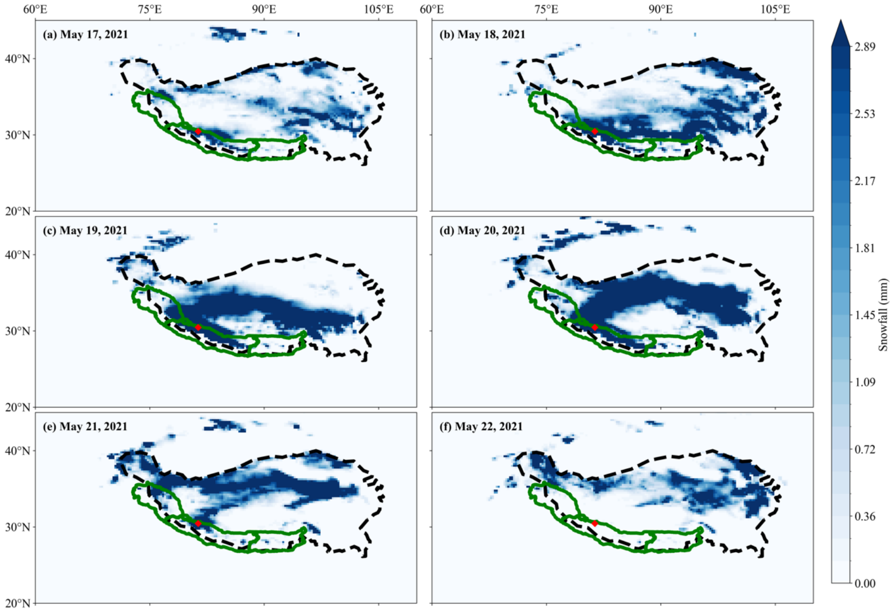

**Figure 9: Spatial distribution of daily snowfall from ERA5 data over the Tibetan Plateau and surrounding regions from May 17 to 22, 2021. The black dashed line denotes the boundary of the Tibetan Plateau, while the green solid line represents the extent and subdivision of the Himalayas. The red diamond markers**

**indicate the location of Naimona'nyi Glacier. Panels (a)–(f) correspond to May 17–22, 2021, respectively.**

### 5.2 Multivariate validation of the impact range of tropical cyclone Tauktae

To further verify the spatial extent of the impacts of TC Tauktae, daily anomalies of precipitation, cloud fraction, radiation-related variables and RH were calculated from ERA5 data for May 18–21, 2021, relative to the baseline period (Fig. 10). The precipitation, cloud fraction, and RH anomalies (Fig. S13) exhibited clear spatiotemporal evolution. On May 18, 2021, significant positive anomalies were mainly concentrated over the central Himalayas, while anomalies in the eastern Himalayas were relatively weak. During May 19–20, 2021, the positive anomalies expanded eastward and covered the central and most of the eastern Himalayas. By May 21, 2021, the affected area had substantially contracted, with pronounced positive anomalies remaining only in limited parts of the central Himalayas. The radiation variables showed a similar spatiotemporal pattern. Anomalies in $S_{net}$ and $S_{in}$ were characterized by widespread negative values across the central and eastern Himalayas during May 18–20, 2021. By May 21, 2021, the negative anomalies had weakened considerably and were mainly confined to the central Himalayas. Meanwhile, albedo and snowfall anomalies were predominantly positive over the central Himalayas throughout May 18–21, 2021 (Fig. 10). This spatial pattern is generally consistent with the albedo and snowfall changes during the TC period, indicating a weaker albedo response in the eastern Himalayas, associated with limited snow cover. Isotope-based studies also indicate that the moisture transported to the TP is influenced by large-scale circulation (Gao et al., 2026). Accordingly, the meteorological and energy perturbations associated with TC Tauktae mainly affected the central and eastern Himalayas, reaching their maximum intensity during May 19–20, 2021.

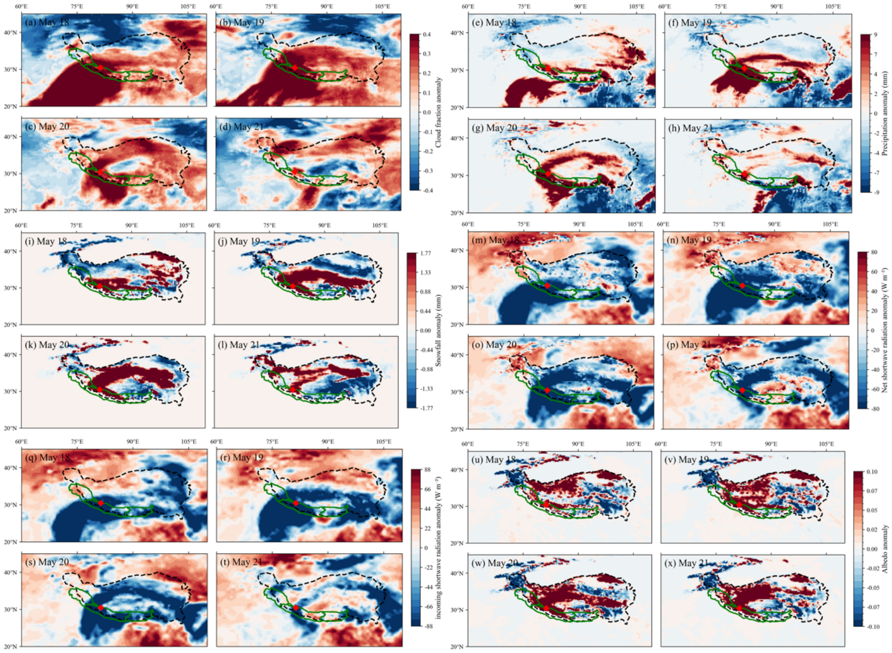

**Figure 10: Daily anomalies of meteorological variables over the Tibetan Plateau during May 18–21, 2021. Panels show (a–d) cloud fraction (%), (e–h) precipitation (mm), (i–l) snowfall (mm), (m–p) net shortwave radiation ($S_{net}$, W m⁻²), (q–t) incoming shortwave radiation ($S_{in}$, W m⁻²), and (u–x) surface albedo. Anomalies are calculated relative to the 2000–2024 climatology for the corresponding day of the year. The black dashed line indicates the Tibetan Plateau boundary, green outlines denote the Himalaya region, and the red diamond marks the location of Naimona'nyi Glacier.**

### 5.3 Multiple impacts of tropical cyclones on glacierized regions

Tropical cyclones are commonly accompanied by intense precipitation and can exert dual impacts on high-mountain environments and glacio-hydrological processes. In high-altitude regions, precipitation often falls as snow and is temporarily stored in glacierized areas in solid form. During the subsequent ablation season, this snow is gradually melted and released, helping to sustain the stability of downstream river discharge, thereby partially alleviating seasonal water scarcity (Pritchard, 2019; Ultee et al., 2022). On the other hand, during the intense ablation season, deposited snow can increase surface albedo and reduce $S_{net}$, thereby suppressing rapid glacier melt and lowering the risk of extreme meltwater events. Moreover, snowfall events may also have adverse impacts on high-mountain ecosystems and human activities. In high-altitude pastoral regions, heavy snowfall can disrupt transportation networks and negatively affect pastoral production and livestock survival, and in some cases may even lead to livestock mortality (Li et al., 2018). In addition, snow anomalies produce thick snow cover that serves as a mass source for avalanches, and through snow entrainment, they increase avalanche volume and lubricate avalanche movement, thereby exacerbating avalanche hazards (Bartelt et al., 2016; Vera Valero et al., 2018; Zhuang et al., 2024). Under a changing climate, studies suggest that the intensity of tropical cyclones may increase in the future (Swapna et al., 2022; Vidya et al., 2023). Therefore, it is important to enhance our understanding of the mechanisms by which TC influences glacier mass balance and regional hazard risk, as well as to improve related assessments.

## 6. Conclusion

This study used observational meteorological data and an energy–mass balance model to simulate the energy and mass balance of Naimona'nyi Glacier from 2000 to 2024, and to analyze the impacts of TC Tauktae and the underlying mechanisms driving glacier changes in May 2021.

Results indicate that the TC Tauktae caused pronounced meteorological anomalies during the TC period, with precipitation, RH, and WS reaching the highest values recorded for the corresponding calendar period since 2000, accompanied by increases in $T_a$ and cloud cover. Under these conditions, $S_{in}$ decreased while albedo increased, resulting in a 37.6 W m$^{-2}$ decrease in $S_{net}$. These changes reduced melt energy by 5.4 W m$^{-2}$ and glacier melt by 1.4 mm w.e. d$^{-1}$. At the same time, increases in RH weakened $H_{lat}$, reducing sublimation by 0.12 mm w.e. d$^{-1}$. Moreover, nearly all precipitation fell as snow, adding 5.6 mm w.e. d$^{-1}$ to glacier mass accumulation. The combined effects of these processes led to a markedly positive mass balance across the entire glacier during the TC period. Moreover, these meteorological and energy anomalies were not confined to Naimona'nyi Glacier. The spatial distributions and anomalies of meteorological and energy variables derived from ERA5 data indicate that the influence of the cyclone extended to the central–eastern Himalayas.

The formation and intensity of TCs are controlled by ocean–atmosphere conditions, and this study is the first to reveal how TCs affect glacier mass balance. However, under the context of climate change, TC activity is likely to intensify in the future, potentially amplifying its impacts on glaciers. Therefore, to better understand the potential effects of tropical cyclones on glacier change, systematic studies across different regions and temporal scales are necessary, alongside enhanced long-term observations and monitoring, which will provide critical support for glacier change assessments and water resource management.

**Code/Data availability** The ERA5 data used in this study are available from the Copernicus Climate Data Store at https://cds.climate.copernicus.eu/datasets. The DEM data were obtained from the Open Topography data portal at https://portal.opentopography.org/dataCatalog.

**Author contribution** ZFY: data curation, formal analysis, visualization, writing (original draft preparation). GXL: data curation, writing (review and editing). BSH: data curation, resources. ZJ: data curation. GJ: conceptualization, supervision, project administration. LR: data curation, formal analysis. ZML: conceptualization, methodology, supervision, writing (review and editing), field observations, funding acquisition. ZHB: field observations, data curation.

**Competing interests** The authors declare that they have no conflict of interest.

**Financial support** This study is jointly funded by the National Key Research and Development Program of China (Grant No. 2024YFF0808601), the Science and Technology Projects of Xizang Autonomous Region, China (XZ202501JD0025 and XZ202501ZY0081), the Second Tibetan Plateau Scientific Expedition and Research Program (2024QZKK0400 and 2024QZKK0100), and the National Natural Science Foundation of China (Grant No. 42471142).

## References

Ali, A.: Climate change impacts and adaptation assessment in Bangladesh, Climate Research, 12, 109–116, https://doi.org/10.3354/cr012109, 1999.

Bartelt, P., Buser, O., Valero, C. V., and Bühler, Y.: Configurational energy and the formation of mixed flowing/powder snow and ice avalanches, Annals of Glaciology, 57, 179–188, https://doi.org/10.3189/2016AoG71A464, 2016.

Bhardwaj, P., Pattanaik, D. R., and Singh, O.: Tropical cyclone activity over Bay of Bengal in relation to El Niño-Southern Oscillation, International Journal of Climatology, 39, 5452–5469, https://doi.org/10.1002/joc.6165, 2019.

Chen, J., Xue, X., and Du, W.: Short communication: Extreme glacier mass loss triggered by high temperature and drought during hydrological year 2022 / 2023 in Qilian Mountains, Research in Cold and Arid Regions, 16, 1–4, https://doi.org/10.1016/j.rcar.2024.01.002, 2024.

Conway, J. P. and Cullen, N. J.: Cloud effects on surface energy and mass balance in the ablation area of Brewster Glacier, New Zealand, The Cryosphere, 10, 313–328, https://doi.org/10.5194/tc-10-313-2016, 2016.

Dare, R. A., Davidson, N. E., and McBride, J. L.: Tropical Cyclone Contribution to Rainfall over Australia, Monthly Weather Review, 140, 3606–3619, https://doi.org/10.1175/MWR-D-11-00340.1, 2012.

Davies, B. J., Golledge, N. R., Glasser, N. F., Carrivick, J. L., Ligtenberg, S. R. M., Barrand, N. E., van den Broeke, M. R., Hambrey, M. J., and Smellie, J. L.: Modelled glacier response to centennial temperature and precipitation trends on the Antarctic Peninsula, Nature Climate Change, 4, 993–998, https://doi.org/10.1038/nclimate2369, 2014.

DeGaetano, A. T. and Allen, R. J.: Trends in Twentieth-Century Temperature Extremes across the United States, Journal of Climate, 15, 3188–3205, https://doi.org/10.1175/1520-0442(2002)015%3C3188:TITCTE%3E2.0.CO;2, 2002.

Duan, K., Yao, T., Wang, N., Shi, P., and Meng, Y.: Changes in equilibrium-line altitude and implications for glacier evolution in the Asian high mountains in the 21st century, Science China Earth Sciences, 65, 1308–1316, https://doi.org/10.1007/s11430-021-9923-6, 2022.

Emanuel, K.: Tropical Cyclones, Annual Review of Earth and Planetary Sciences, 31, 75–104, https://doi.org/10.1146/annurev.earth.31.100901.141259, 2003.

Felton, C. S., Subrahmanyam, B., and Murty, V. S. N.: ENSO-Modulated Cyclogenesis over the Bay of Bengal, Journal of Climate, 26, 9806–9818, https://doi.org/10.1175/JCLI-D-13-00134.1, 2013.

Fujita, K. and Ageta, Y.: Effect of summer accumulation on glacier mass balance on the Tibetan Plateau revealed by mass-balance model, Journal of Glaciology, 46, 244–252, https://doi.org/10.3189/172756500781832945, 2000.

Gao, J., Yao, T., Masson-Delmotte, V., Steen-Larsen, H. C., and Wang, W.: Collapsing glaciers threaten Asia's water supplies, Nature, 565, 19–21, 2019.

Gao, J., Yao, T., Masson-Delmotte, V., Werner, M., Jouzel, J., Thompson, L., Casado, M., Steen-Larsen, H. C., Cauquoin, A., Mosley-Thompson, E., He, Z., Cai, R., Zhang, T., Liu, Y., Chen, G., Xu, B., Wu, G., Pang, H., and He, M.: Vertical conveyor driving the integration of moisture transported by the westerlies to the Asian water towers' atmospheric water cycle, Proceedings of the National Academy of Sciences, 123, e2529749123, https://doi.org/10.1073/pnas.2529749123, 2026.

Guo, W., Liu, S., Xu, J., Wu, L., Shangguan, D., Yao, X., Wei, J., Bao, W., Yu, P., Liu, Q., and Jiang, Z.: The second Chinese glacier inventory: data, methods and results, Journal of Glaciology, 61, 357–372, https://doi.org/10.3189/2015JoG14J209, 2015.

Hock, R. and Holmgren, B.: A distributed surface energy-balance model for complex topography and its application to Storglaciären, Sweden, Journal of Glaciology, 51, 25–36, https://doi.org/10.3189/172756505781829566, 2005.

Jouberton, A., Shaw, T. E., Miles, E., McCarthy, M., Fugger, S., Ren, S., Dehecq, A., Yang, W., and Pellicciotti, F.: Warming-induced monsoon precipitation phase change intensifies glacier mass loss in the southeastern Tibetan Plateau, Proceedings of the National Academy of Sciences, 119, e2109796119, https://doi.org/10.1073/pnas.2109796119, 2022.

Kääb, A., Berthier, E., Nuth, C., Gardelle, J., and Arnaud, Y.: Contrasting patterns of early twenty-first-century glacier mass change in the Himalayas, Nature, 488, 495–498, https://doi.org/10.1038/nature11324, 2012.

Kang, S., Chen, F., Gao, T., Zhang, Y., Yang, W., Yu, W., and Yao, T.: Early onset of rainy season suppresses glacier melt: a case study on Zhadang glacier, Tibetan Plateau, Journal of Glaciology, 55, 755–758, https://doi.org/10.3189/002214309789470978, 2009.

Kannaujiya, V. K., Rai, A. K., and Malakar, S.: Nature and impact of extremely severe cyclone Tauktae over India, Discover Oceans, 1, 4, https://doi.org/10.1007/s44289-024-00004-x, 2024.

Khouakhi, A., Villarini, G., and Vecchi, G. A.: Contribution of Tropical Cyclones to Rainfall at the Global Scale, Journal of Climate, 30, 359–372, https://doi.org/10.1175/JCLI-D-16-0298.1, 2017.

Krishnamohan, K. S., Mohanakumar, K., and Joseph, P. V.: The influence of Madden–Julian Oscillation in the genesis of North Indian Ocean tropical cyclones, Theoretical and Applied

Climatology, 109, 271–282, https://doi.org/10.1007/s00704-011-0582-x, 2012.

Kropač, E., Mölg, T., Cullen, N. J., Collier, E., Pickler, C., and Turton, J. V.: A Detailed, Multi-Scale Assessment of an Atmospheric River Event and Its Impact on Extreme Glacier Melt in the Southern Alps of New Zealand, Journal of Geophysical Research: Atmospheres, 126, e2020JD034217, https://doi.org/10.1029/2020JD034217, 2021.

Li, Y., Ye, T., Liu, W., and Gao, Y.: Linking livestock snow disaster mortality and environmental stressors in the Qinghai-Tibetan Plateau: Quantification based on generalized additive models, Science of The Total Environment, 625, 87–95, https://doi.org/10.1016/j.scitotenv.2017.12.230, 2018.

Luo, D., Lin, D., Xu, Y., Zhu, M., Zhu, F., Zhao, H., and Xiang, Y.: The processes and impacts of drought-induced extreme glacier mass loss on the south-central Tibetan Plateau, Journal of Hydrology, 675, 135645, https://doi.org/10.1016/j.jhydrol.2026.135645, 2026.

Milner, A. M., Khamis, K., Battin, T. J., Brittain, J. E., Barrand, N. E., Füreder, L., Cauvy-Fraunié, S., Gíslason, G. M., Jacobsen, D., Hannah, D. M., Hodson, A. J., Hood, E., Lencioni, V., Ólafsson, J. S., Robinson, C. T., Tranter, M., and Brown, L. E.: Glacier shrinkage driving global changes in downstream systems, Proceedings of the National Academy of Sciences, 114, 9770–9778, https://doi.org/10.1073/pnas.1619807114, 2017.

Mote, T.: Atmospheric and oceanic climate forcing of the exceptional Greenland ice sheet surface melt in summer 2012, International Journal of Climatology, https://doi.org/10.1002/JOC.3743, 2014.

Nerantzaki, S. D. and Papalexiou, S. M.: Assessing extremes in hydroclimatology: A review on probabilistic methods, Journal of Hydrology, 605, 127302, https://doi.org/10.1016/j.jhydrol.2021.127302, 2022.

van Pelt, W. J. J., Oerlemans, J., Reijmer, C. H., Pohjola, V. A., Pettersson, R., and Van Angelen, J. H.: Simulating melt, runoff and refreezing on Nordenskiöldbreen, Svalbard, using a coupled snow and energy balance model, The Cryosphere, 6, 641–659, https://doi.org/10.5194/tc-6-641-2012, 2012.

van Pelt, W., Pohjola, V., Pettersson, R., Marchenko, S., Kohler, J., Luks, B., Hagen, J. O., Sc huler, T. V., Dunse, T., Noël, B., and Reijmer, C.: A long-term dataset of climatic mass balance, snow conditions, and runoff in Svalbard (1957–2018), The Cryosphere, 13, 2259–2280, https://doi.org/10.5194/tc-13-2259-2019, 2019.

Pritchard, H. D.: Asia's shrinking glaciers protect large populations from drought stress, Nature, 569, 649–654, https://doi.org/10.1038/s41586-019-1240-1, 2019.

Ratnakaran, A. P. and Abish, B.: Role of warm ocean conditions in the genesis and rapid intensification of tropical cyclone 'Tauktae' along the west coast of India, Theoretical and Applied Climatology, 153, 417–430, https://doi.org/10.1007/s00704-023-04480-7, 2023.

Ren, F., Wu, G., Dong, W., Wang, X., Wang, Y., Ai, W., and Li, W.: Changes in tropical cyclone precipitation over China, Geophysical Research Letters, 33, https://doi.org/10.1029/2006GL027951, 2006.

Schär, C., Ban, N., Fischer, E. M., Rajczak, J., Schmidli, J., Frei, C., Giorgi, F., Karl, T. R., Kendon, E. J., Tank, A. M. G. K., O'Gorman, P. A., Sillmann, J., Zhang, X., and Zwiers, F. W.: Percentile indices for assessing changes in heavy precipitation events, Climatic Change, 137, 201–216, https://doi.org/10.1007/s10584-016-1669-2, 2016.

Singh, V. K. and Roxy, M. K.: A review of ocean-atmosphere interactions during tropical cyclones in the north Indian Ocean, Earth-Science Reviews, 226, 103967, https://doi.org/10.1016/j.earscirev.2022.103967, 2022.

Singh, V. K., Roxy, M. K., and Deshpande, M.: The unusual long track and rapid intensification of very severe cyclone Ockhi, Current Science, 119, 771–779, 2020.

Swapna, P., Sreeraj, P., Sandeep, N., Jyoti, J., Krishnan, R., Prajeesh, A. G., Ayantika, D. C., and Manmeet, S.: Increasing Frequency of Extremely Severe Cyclonic Storms in the North Indian Ocean by Anthropogenic Warming and Southwest Monsoon Weakening, Geophysical Research Letters, 49, e2021GL094650, https://doi.org/10.1029/2021GL094650, 2022.

Thibert, E., Dkengne Sielenou, P., Vionnet, V., Eckert, N., and Vincent, C.: Causes of Glacier Melt Extremes in the Alps Since 1949, Geophysical Research Letters, 45, 817–825, https://doi.org/10.1002/2017GL076333, 2018.

Ultee, L., Coats, S., and Mackay, J.: Glacial runoff buffers droughts through the 21st century, Earth System Dynamics, 13, 935–959, https://doi.org/10.5194/esd-13-935-2022, 2022.

Umakanth, N., Kumar, P. V., Biswasharma, R., Gogineni, R., Ahammad, S. H., and Rao, M. C.: Association of Mesoscale Features With Tropical Cyclone Tauktae, Thalassas, 40, 1521–1543, https://doi.org/10.1007/s41208-024-00740-z, 2024.

Vera Valero, C., Wever, N., Christen, M., and Bartelt, P.: Modeling the influence of snow cover temperature and water content on wet-snow avalanche runout, Natural Hazards and Earth System Sciences, 18, 869–887, https://doi.org/10.5194/nhess-18-869-2018, 2018.

Vidya, P. J., Chatterjee, S., Ravichandran, M., Gautham, S., Nuncio, M., and Murtugudde, R.: Intensification of Arabian Sea cyclone genesis potential and its association with Warm Arctic Cold Eurasia pattern, npj Climate and Atmospheric Science, 6, 146, https://doi.org/10.1038/s41612-023-00476-2, 2023.

VinodKumar, K., Soumya, M., Tkalich, P., and Vethamony, P.: Ocean-atmosphere interaction during Thane cyclone: A numerical study using WRF, Indian Journal of Geo-Marine Sciences, 2014.

Vuille, M., Kaser, G., and Juen, I.: Glacier mass balance variability in the Cordillera Blanca, Peru and its relationship with climate and the large-scale circulation, Global and Planetary Change, 62, 14–28, https://doi.org/10.1016/j.gloplacha.2007.11.003, 2008.

Wang, N., Yao., T., Xu, B., Chen, A., and Wang, W.: Spatiotemporal Pattern, Trend, and Influence of Glacier Change in Tibetan Plateau and Surroundings under Global Warming, Bulletin of Chinese Academy of Sciences, 34, 1220–1232, https://doi.org/10.16418/j.issn.1000-3045.2019.11.005, 2019.

White, R. H., Anderson, S., Booth, J. F., Braich, G., Draeger, C., Fei, C., Harley, C. D. G., Henderson, S. B., Jakob, M., Lau, C.-A., Mareshet Admasu, L., Narinesingh, V., Rodell, C., Roocroft, E., Weinberger, K. R., and West, G.: The unprecedented Pacific Northwest heatwave of June 2021, Nature Communications, 14, 727, https://doi.org/10.1038/s41467-023-36289-3, 2023.

Xu, C., Li, H., Wang, F., Li, Z., Zhou, P., and Liu, S.: Heatwaves in summer 2022 forces substantial mass loss for Urumqi Glacier No. 1, China, Journal of Glaciology, 70, e77, https:/

/doi.org/10.1017/jog.2024.4, 2024.

Yang, W., Yao, T., Guo, X., Zhu, M., Li, S., and Kattel, D. B.: Mass balance of a maritime glacier on the southeast Tibetan Plateau and its climatic sensitivity, Journal of Geophysical Research: Atmospheres, 118, 9579–9594, https://doi.org/10.1002/jgrd.50760, 2013.

Yao, T., Wang, Y., Liu, S., Pu, J., Shen, Y., and Lu, A.: Recent glacial retreat in High Asia in China and its impact on water resource in Northwest China, Science in China Series D: Earth Sciences, 47, 1065–1075, https://doi.org/10.1360/03yd0256, 2004.

Yao, T., Thompson, L., Yang, W., Yu, W., Gao, Y., Guo, X., Yang, X., Duan, K., Zhao, H., Xu, B., Pu, J., Lu, A., Xiang, Y., Kattel, D. B., and Joswiak, D.: Different glacier status with atmospheric circulations in Tibetan Plateau and surroundings, Nature Climate Change, 2, 663–667, https://doi.org/10.1038/nclimate1580, 2012.

Yao, T., Bolch, T., Chen, D., Gao, J., Immerzeel, W., Piao, S., Su, F., Thompson, L., Wada, Y., Wang, L., Wang, T., Wu, G., Xu, B., Yang, W., Zhang, G., and Zhao, P.: The imbalance of the Asian water tower, Nature Reviews Earth & Environment, 3, 618–632, https://doi.org/10.1038/s43017-022-00299-4, 2022.

You, C., Wang, J., Lin, R., and Xu, C.: Vegetation Fire Emissions Exacerbate Glacier Melting on the Third Pole, Environmental Science & Technology, 59, 3046–3053, https://doi.org/10.1021/acs.est.4c08090, 2025.

Zahid, G. G. and Harikumar, R.: On the reasons and quantified prevalent ocean atmosphere roles for the intensification and genesis features of the ESCS Tauktae, Scientific Reports, 15, 7482, https://doi.org/10.1038/s41598-025-92460-4, 2025.

Zhang, H., Li, Z., Zhou, P., Zhu, X., and Wang, L.: Mass-balance observations and reconstruction for Haxilegen Glacier No.51, eastern Tien Shan, from 1999 to 2015, Journal of Glaciology, 64, 689–699, https://doi.org/10.1017/jog.2018.58, 2018.

Zhang, Y., Hirabayashi, Y., and Liu, S.: Catchment-scale reconstruction of glacier mass balance using observations and global climate data: Case study of the Hailuogou catchment, south-eastern Tibetan Plateau, Journal of Hydrology, 444–445, 146–160, https://doi.org/10.1016/j.jhydrol.2012.04.014, 2012.

https://doi.org/10.5194/egusphere-2026-3661
Preprint. Discussion started: 7 July 2026

Zhang, Y., Gao, T., Kang, S., Shangguan, D., and Luo, X.: Albedo reduction as an important driver for glacier melting in Tibetan Plateau and its surrounding areas, Earth-Science Reviews, 220, 103735, https://doi.org/10.1016/j.earscirev.2021.103735, 2021.

Zhao, H., Yang, W., Yao, T., Tian, L., and Xu, B.: Dramatic mass loss in extreme high-elevation areas of a western Himalayan glacier: observations and modeling, Scientific Reports, 6, 30706, https://doi.org/10.1038/srep30706, 2016.

Zhu, F., Zhu, M., Yang, W., Wang, Z., Guo, Y., and Yao, T.: Drivers of the Extreme Early Spring Glacier Melt of 2022 on the Central Tibetan Plateau, Earth and Space Science, 11, e2023EA003297, https://doi.org/10.1029/2023EA003297, 2024.

Zhu, M., Yang, W., Yao, T., Tian, L., Thompson, L. G., and Zhao, H.: The Influence of Key Climate Variables on Mass Balance of Naimona'nyi Glacier on a North-Facing Slope in the Western Himalayas, Journal of Geophysical Research: Atmospheres, 126, e2020JD033956, https://doi.org/10.1029/2020JD033956, 2021.

Zhu, M., Yao, T., Yang, W., Wu, G., Li, S., Zhao, H., and Thompson, L. G.: Possible Causes of Anomalous Glacier Mass Balance in the Western Kunlun Mountains, Journal of Geophysical Research: Atmospheres, 127, e2021JD035705, https://doi.org/10.1029/2021JD035705, 2022.

Zhu, M., Thompson, L. G., Yao, T., Jin, S., Yang, W., Xiang, Y., and Zhao, H.: Opposite mass balance variations between glaciers in western Tibet and the western Tien Shan, Global and Planetary Change, 220, 103997, https://doi.org/10.1016/j.gloplacha.2022.103997, 2023.

Zhu, M., Yao, T., Thompson, L. G., Yang, W., Zhu, F., Lin, D., Zhong, Z.-P., Zhao, H., Zhang, X., and Li, S.: Linking Northeastern Indian Subcontinental High Temperature to Extreme Glacier Mass Loss on the South-Central Tibetan Plateau, Journal of Geophysical Research: Atmospheres, 131, e2025JD045031, https://doi.org/10.1029/2025JD045031, 2026a.

Zhu, M., Wang, S., Gao, X., Zhang, F., Zhu, F., and Zhao, H.: Reduced glacier mass loss rates on the southern Tibetan Plateau during a global warming hiatus, Global and Planetary Change, 262, 105476, https://doi.org/10.1016/j.gloplacha.2026.105476, 2026b.

Zhuang, Y., Dawadi, B., Steiner, J., Dash, R. K., Bühler, Y., Munch, J., and Bartelt, P.: An ea rthquake-triggered avalanche in Nepal in 2015 was exacerbated by climate variability and snowfall anomalies, Communications Earth & Environment, 5, 465, https://doi.org/10.1038/s43247-024-01624-z, 2024.